Reactivities of 1,2-, 1,3-, and 1,4-Dihydroxynaphthalenes toward Electrogenerated Superoxide in *N*,*N*-Dimethylformamide through Proton-coupled Electron Transfer

Tatsushi Nakayama,[*,†] and *Bunji Uno,*[‡]

[†]Department of Pharmacy, Gifu Pharmaceutical University, 1-25-4 Daigaku-nishi, Gifu, 501–1196, Japan

[‡]Faculty of Pharmacy, Gifu University of Medical Science, 4-3-3 Nijigaoka, Kani, Gifu 509–0923, Japan

*Phone: +81-58-230-8100 Fax: +81-58-230-8200 E-mail: tnakayama@gifu-pu.ac.jp

Abstract

We have carried out an electrochemical and theoretical study on the reactivity of 1,2-, 1,3-, and 1,4-dihydroxynaphthalenes (1*n*H_2NQ, *n* = 2, 3, 4) toward electrogenerated superoxide radical anion ($O_2^{\bullet-}$) in *N*,*N*-dimethylformamide. Cyclicvoltammetry and in situ electrolytic electron spin resonance measurements revealed that the quinone–hydroquinone π-conjugation plays an important role in a successful $O_2^{\bullet-}$ scavenging by 12H_2NQ and 14H_2NQ through proton-coupled electron transfer (PCET) reaction. The reactivities of 12H_2NQ and 14H_2NQ toward $O_2^{\bullet-}$ were mediated by the ortho- (catechol) or para-diphenol (hydroquinone) moieties,

as experimentally confirmed in comparative analyses with catechol, hydroquinone, and 13H_2NQ, aided by density functional theory (DFT) calculations. The electrochemical and DFT results suggested that a concerted PCET mechanism involving two-proton transfers and one-electron transfer proceeds with a superior kinetic, demonstrating a successful $O_2^{\bullet-}$ scavenging by 12H_2NQ and 14H_2NQ. Furthermore, a subsequent electron transfer between molecular dioxygen and product-naphthoquinone-radicals was observed, where $O_2^{\bullet-}$ was generated. The DFT analysis suggested that the spin distribution on the planar naphthalene ring embodies the superior kinetics of the PCET and the subsequent generation of $O_2^{\bullet-}$ from dioxygen demonstrated in the electrochemical results.

1 Introduction

Dihydroxynaphthalene (H_2NQ) is a type of phenolic compound that has two hydroxyl groups (OH) on its naphthalene ring, where nine isomers exist. Its derivatives are found in various natural and industrial compounds such as phenolic antioxidants, vitamin K-group, drug materials.[1–4] Especially, some of them whose molecular skelton can be oxidized to quinoid structure with its resonance effect show a surprising number of health benefits and pharmacological properties, such as cytotoxic, antibacterial, antifungal, antiviral, cardioprotective, anti-ischemic, hepatoprotective, neuroprotective, and antitumoral.[1,5–7] Conversely, members of this family of compounds also include harmful environmental contaminants. The harmful effects of H_2NQ on living organisms are thought to be due to cytotoxicity and at the same time to be related to antitumor activities.[5–9] These diverse reactivities are mainly caused by the redox activities of naphthoquinone (NQ), oxidized form of 1,*n*-dihydroxynaphthalenes (1*n*H_2NQ, *n* = 2, 3, 4) having two OHs on the same ring. NQ is a planar molecule with one aromatic ring fused to a quinone subunit. Like benzoquinone or ubiquinone (mono ring), ortho- and para- NQ (naphthalene-1,2-dione:12NQ and naphthalene-1,4-dione:14NQ) can come in several redox states: radical anion ($NQ^{\bullet-}$), semiquinone radical

(HNQ$^{\bullet}$), and H_2NQ, along the quinone–hydroquinone π-conjugated reaction. However, it is unclear which redox species substantially exhibits which bioreactive effect with its mechanism of action.

Meanwhile, special attention has been directed to the anticancer action and potential therapeutic significance of natural and synthetic quinones involving NQs (H_2NQ) such as lapachol, juglone, and menadione.[1,4,6,8,10] Some of the most important explored so far which have been extendedly reported are the damage of DNA through the generation of reactive oxygen species (ROS), inhibition of topoisomerase II, regulation of the tumor suppressor factor p53 and induction of apoptosis via endoplasmic reticulum stress. Within this framework, different reaction mechanisms have been proposed to explain the NQ anticancer activity. Some papers have concluded that the antitumoral activity of these compounds is related to drug-DNA intercalation with the direct intervention of anionic intermediaries (naphthoquinone radicl anion:$NQ^{\bullet-}$ and naphthoquinone dianion NQ^{2-}) which are produced by electron capture during the bioreductive transformation of quinones.[11,12] Under aerobic conditions, the anionic intermediaries can transfer an electron to the molecular oxygen (O_2) to yield the original quinone and the reduced O_2, superoxide radical anion ($O_2^{\bullet-}$). Furthermore, it spontaneously disproportionates to produce O_2 and hydrogen peroxide (H_2O_2), which, in the presence of ferrous ion, yields the highly reactive and toxic hydroxyl radical (HO$^{\bullet}$) species through the Fenton reaction.[13–15] In any or both scenarios, NQs act as anticancer agents through various mechanisms involved in all types of cancer, although they are now considered too toxic for use since once studied as a possible treatment for some types of cancer. There is still a lot to be elucidated about the ways in which NQs exert their action as anticancer agents and how to enhance their activity in order to exploit their potential to the maximum. Therefore, NQ-type systems are still an important and attractive subject in biology

and chemistry, due to their biological activity that depends on structural features and redox properties.

It is well recognized that the quinone and NQ derivatives induce oxidative stress generating $O_2^{\bullet-}$.[16,17] Simultaneously, 12H_2NQ and 14H_2NQ (reduced forms of 12NQ and 14NQ) function as also antioxidants by reducing ROS, forming their oxidized forms. That is, the NQ-type system possibly causes both ROS-generation and ROS-scavenging related to the redox states of 12H_2NQ and 14H_2NQ. Therefore, it is necessary to demonstrate the chemical reaction mechanism including electron transfer (ET) between 1*n*H_2NQ and the ROS with the following reaction of their products, to infer the biochemical and medicinal effect. That is, clarifying the mechanism between 1*n*H_2NQ and the ROS, $O_2^{\bullet-}$, hydroperoxyl radical ($HO_2^{\bullet}$), and $HO^{\bullet}$, is a prerequisite to elucidate the related biochemical effect.

Among the possible mechanisms of ROS ($O_2^{\bullet-}$, $HO^{\bullet}$, and $HO_2^{\bullet}$) scavenging by 1*n*H_2NQ and other phenolic antioxidants are single ET, superoxide-facilitated oxidation (SFO),[18–20] hydrogen atom transfer (HAT) involving proton-coupled electron transfer (PCET),[21–25] and sequential proton-loss electron transfer.[26] In the SFO mechanism, $HO_2^{\bullet}$ is generated by initial proton transfer (PT) from the substrate to $O_2^{\bullet-}$ and undergoes rapid dismutation into H_2O_2 and O_2. The O_2 formed in the dismutation process then oxidizes the substrate anion.[27] The other mechanisms involve direct oxidation by ROS. Previously, we reported that electrogenerated $O_2^{\bullet-}$ is scavenged by polyphenols,[24] 1,2- and 1,4- benzendiols (catechol[22] and hydroquinone[23]), and monophenols including aminophenols[25,28] and tocopherols[29] through the PCET. In these studies, the PCET mechanism for successful $O_2^{\bullet-}$ scavenging was mediated by quinone–hydroquinone π-conjugation and involved two PTs and one ET. Accordingly, a plausible main mechanism for $O_2^{\bullet-}$ scavenging by 12H_2NQ/14H_2NQ is simply denoted in Scheme 1, forming 12$NQ^{\bullet-}$/14$NQ^{\bullet-}$ and H_2O_2 as products. $O_2^{\bullet-}$, a precursor of other ROS, does not readily accept electrons from 1*n*H_2NQ, but $HO_2^{\bullet}$ formed through

protonation of $O_2^{\bullet-}$ as a Brønsted base is a strong oxidant with a short lifetime. Thus, the deprotonation (PT) is closely related to the subsequent oxidation (ET) along the PCET between 1*n*H_2NQ/anions and $O_2^{\bullet-}$/$HO_2^{\bullet}$, which embodies the actual $O_2^{\bullet-}$/$HO_2^{\bullet}$ scavenging mechanism.

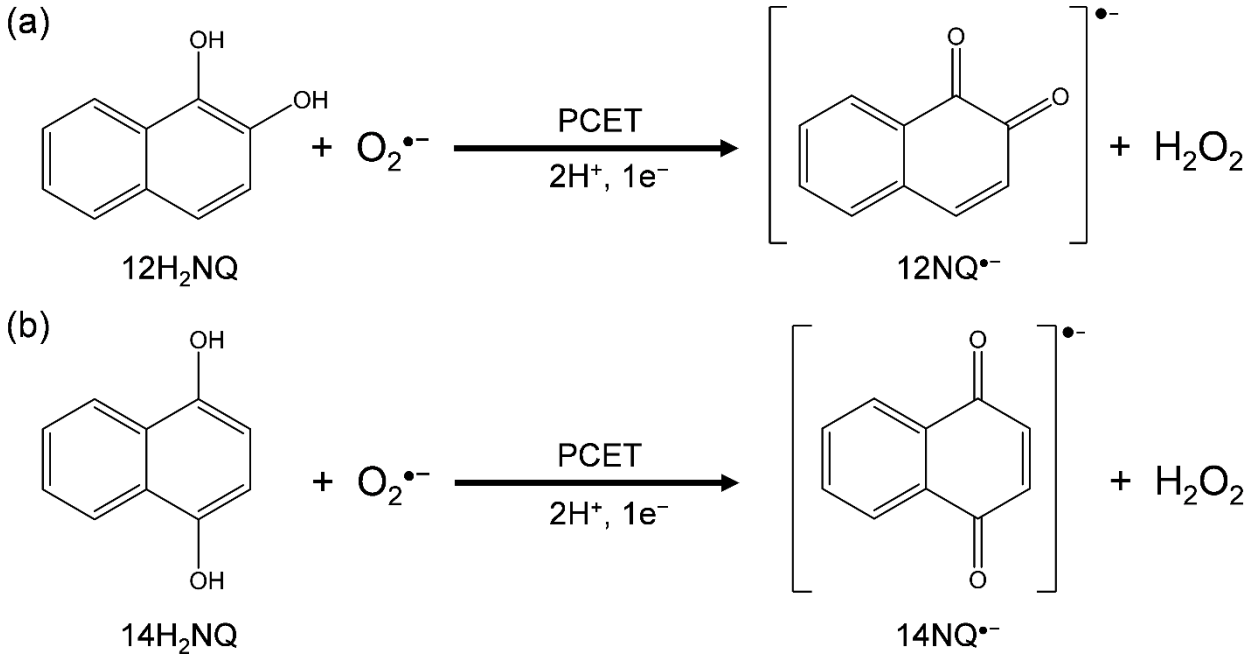

Scheme 1. Plausible reaction schemes of $O_2^{\bullet-}$ scavenging by (a) 12H_2NQ and (b) 14H_2NQ, through proton-coupled electron transfer involving two protons (H^+) and one electron (e^-) transfer.

In the present study, we investigated the chemical reaction between electrogenerated $O_2^{\bullet-}$ and 1*n*H_2NQ in aprotic *N*,*N*-dimethylformamide (DMF) solution. Applying density functional theory (DFT), we also electrochemically investigated the scavenging mechanism of $O_2^{\bullet-}$ by 1*n*H_2NQ and the subsequent reaction of their oxidized product species. The study obtains mechanistic insights into the structural features of 1*n*H_2NQ (1*n*NQ), namely, the ortho- and para- diphenol moiety and the naphthalene ring for π-conjugation. Accordingly, we present valuable information regarding the reactivity between $O_2^{\bullet-}$ and 1*n*H_2NQ, which is assumed to relate to the mechanisms of the ROS-scavenging and ROS-generation. This acquired understanding will enhance the pharmacological use of 1*n*H_2NQ as a drug candidate.

Chart 1. Structures of the compounds considered in the present study

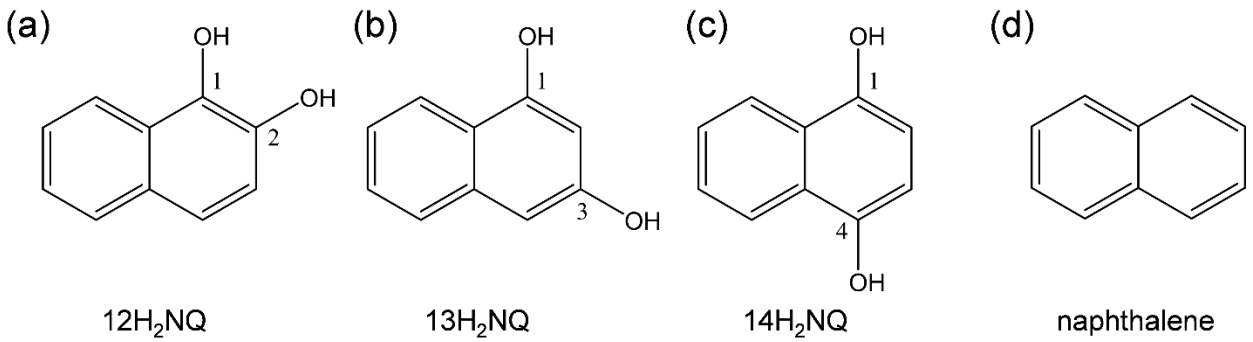

1,*n*-dihydroxynaphthalenes (1*n*H_2NQ), (a) 12H_2NQ, (b) 13H_2NQ, (c) 14H_2NQ, and (d) bicyclo[4.4.0]deca-1,3,5,7,9-pentaene (naphthalene)

2 Materials and methods

2.1 Chemicals

Highest grade 12H_2NQ (>98.0%), 13H_2NQ (>99.0%), 14H_2NQ (>90.0%), and naphthalene (>98.0%) were purchased from Sigma-Aldrich Inc. (Tokyo, Japan) and were used as received. Spectrograde purity DMF (99.7%) as the solvent for electrochemical and electron spin resonance (ESR) spectral measurements was obtained from Nacalai Tesque Inc. (Kyoto, Japan) and used as received. Dinitrogen (N_2) gas (99.0%) and O_2 gas (99.0%) were purchased from Medical Sakai Co., Ltd. (Gifu, Japan), and also used as received. Tetrapropylammonium perchlorate (TPAP, >98.0%) was purchased from Tokyo Chemical Industry Co., Ltd. (Tokyo, Japan) and prepared as described previously.[30] Ferrocene (Fc), used as a potential reference compound, was purchased from Nacalai Tesque Inc. (Kyoto, Japan) and used as received.

2.2 Electrochemical and in situ electrolytic ESR measurements

Cyclic voltammetry was performed in a three-electrode system comprising a 1.0-mm-diameter glassy carbon (GC) working electrode, a coiled platinum (Pt, 99.99%) counter electrode, and a silver/silver nitrate (Ag/$AgNO_3$) reference electrode (containing an acetonitrile solution of 0.1 mol dm^{-3} tetrabutylammonium perchlorate and 0.01 mol dm^{-3} $AgNO_3$). Measurements were collected at 25 °C using an ECstat-301 electrochemical analyzer (EC-frontier Co., Ltd., Kyoto, Japan) coupled to electrochemical software

(Supplementary Materials, Table S1). Prior to the experiments, the working electrode was polished with alumina paste on a polishing wheel and then rinsed with deionized water and acetone. After air drying, the electrode was ready for use. The reference electrode was calibrated with reference to the ferrocenim ion/ferrocene couple (Fc^+/Fc), and all reported potentials are referenced to the potential of the Fc^+/Fc couple. In situ electrolytic ESR spectra were measured using a JES-FA200 X-band spectrometer (JEOL Ltd., Tokyo, Japan). The controlled-potential electrolysis was performed at room temperature in an electrochemical ESR cell using a 0.5-mm-diameter straight Pt wire sealed in a glass capillary as the working electrode (Supplementary Materials, Figure S1). Samples were prepared in a glove box completely filled with N_2 gas to prevent contamination by moisture. The experimental DMF solutions containing 0.1 mol dm^{-3} TPAP as a supporting electrolyte were saturated with O_2 by air-bubbling the gas for ca. 2–3 minutes. To maintain a constant O_2 concentration, the gas was passed over the solutions during the electrochemical and spectral measurements. The equilibrium concentration of O_2 was calculated as 4.8×10^{-3} mol dm^{-3}.

2.3 Theoretical calculations.

All solution-phase calculations were performed at the DFT level with three hybrid functionals, the Becke three-parameter Lee–Yang–Parr (B3LYP), the long-range corrected functionals (ω-B97XD),[31] and the meta exchange-correlated functional (M06-2X),[32] implemented in the Gaussian 16 Program package.[33] These functionals were chosen because they obtain good geometries of the reactants, products, and transition states (TS) in PCET reactions between phenolic compounds and free radicals.[34] The energies of the highest occupied molecular orbital (HOMO) and lowest unoccupied molecular orbital (LUMO) were obtained from geometry optimization with frontier orbital theory. In the geometry optimization, vibrational frequency calculations, intrinsic reaction coordinate (IRC) calculations, and population analysis of each compound, we applied the standard split-

valence triple ζ basis sets augmented by the polarization d,p and diffusion orbitals 6-311+G(d,p). The solvent contribution of DMF to the standard Gibbs free energies was computed by the polarized continuum model (PCM) under the default settings of Gaussian 16. This model is widely employed in thermodynamic characteristic studies of solvation. The internal energies were converted to standard Gibbs energies at 298.15 K using the zero-point energies, thermal correction, and entropy. In the population analysis, the electrons and spins were calculated using the natural bond orbital (NBO) technique.[35]

3. Results and discussion

3.1 Cyclic Voltammetry of $O_2/O_2^{\bullet-}$ in the Presence of 1*n*H_2NQ

Scavenging of electrogenerated $O_2^{\bullet-}$ by the compounds (Chart 1) was inferred from the cyclic voltammograms (CV) of saturated O_2 (4.8×10^{-3} mol dm^{-3}) in DMF (Figure 1). In aprotic and unbuffered solvents such as DMF, O_2 participated in a quasi-reversible redox reaction (Equation (1)) with generation of $O_2^{\bullet-}$ in the initial cathodic scan and reoxidation to the starting materials (O_2) in the returned anodic scan (1c/1a, bold lines in Figure 1). The generated $O_2^{\bullet-}$ was lowly reactive toward aprotic DMF. The reversible CVs investigated here became irreversible in the presence of phenolic compounds (a)–(c) at various concentrations (0 to 5.0×10^{-3} mol dm^{-3}). As the CVs of O_2 in the presence of naphthalene, and of bubbled N_2 showed no peak over the potential range (data is not shown), the loss of reversibility in the CVs of $O_2/O_2^{\bullet-}$ was attributed to an acid–base reaction; specifically, the compound involved in the initial PT to $O_2^{\bullet-}$ acts as a Brønsted base forming $HO_2^{\bullet}$ (Equation (2)).

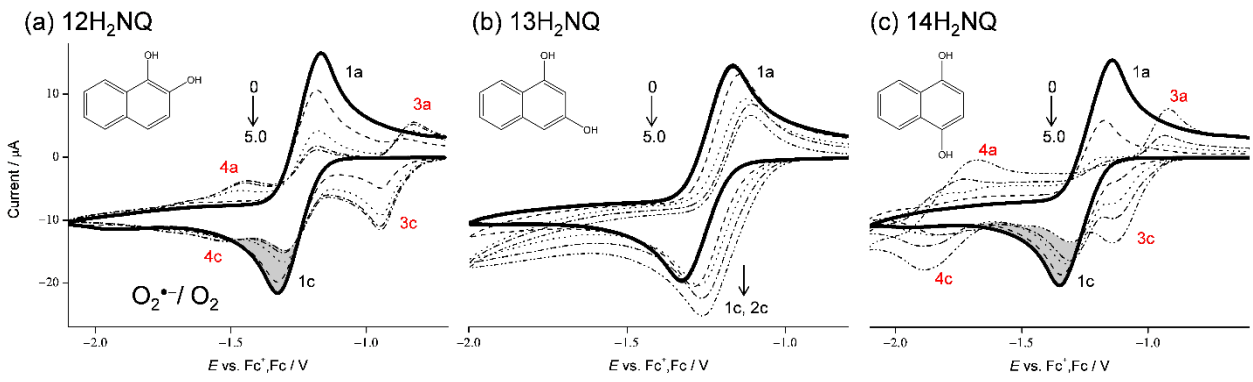

Figure 1. CVs of 4.8×10^{-3} mol dm^{-3} O_2 in the presence of (a) $12H_2NQ$, (b) $13H_2NQ$, and (c) $14H_2NQ$, in DMF containing 0.1 mol dm^{-3} TPAP. All CVs were recorded with a GC electrode at a scan rate of 0.1 V s^{-1}. Concentrations ($\times 10^{-3}$ mol dm^{-3}) are 0, 1.0, 3.0, and 5.0 (arrows indicate the concentration changes).

The generation and consequent reduction of $HO_2^{\bullet}$ (Equation (3)) gave rise to bielectronic CVs in the presence of $13H_2NQ$ (Figure 1b, cathodic current 2c). This bielectronic feature disappeared in the presence of (a) $12H_2NQ$ and (c) $14H_2NQ$ and was replaced by increasing peaks (3c/3a and 4c/4a) caused by scavenging of $HO_2^{\bullet}$ by the subsequent ET, which formed a hydroperoxyl anion (HO_2^-) and substrate radicals ($12HNQ^{\bullet}$ and $14HNQ^{\bullet}$) from the deprotonated anions ($12HNQ^-$ and $14HNQ^-$) (Equation (4)). Consequently, a monoelectronic CV curve appeared.

$$O_2 + e^- \leftrightarrow O_2^{\bullet-} \qquad E^\circ = -1.284 \text{ V vs } Fc^+/Fc \qquad (1)$$

$$O_2^{\bullet-} + 12H_2NQ \rightarrow HO_2^{\bullet} + 12HNQ^- \qquad \text{the initial PT} \qquad (2)$$

$$HO_2^{\bullet} + e^- \rightarrow HO_2^- \qquad E^\circ = -0.4 \text{ to } -0.2 \text{ V vs } Fc^+/Fc \qquad (3)$$

$$HO_2^{\bullet} + 12HNQ^- \rightarrow HO_2^- + 12HNQ^{\bullet} \qquad \text{ET} \qquad (4)$$

$$HO_2^- + 12HNQ^{\bullet} \rightarrow H_2O_2 + 12NQ^{\bullet-} \qquad \text{the second PT} \qquad (5)$$

where E° (V vs Fc^+/Fc) is the standard redox potential.

Based on these results, we rationalized that $O_2^{\bullet-}$ formed after the primary electrode process associated with PT from OH, leading to the irreversible overall reduction of O_2 to H_2O_2 driven by the exergonic reduction of the resulting $HO_2^{\bullet}/HO_2^-$. Therefore, the CV traces of $O_2/O_2^{\bullet-}$ in the presence of $1nH_2NQ$ (Figure 1(a–c)) were divided into two typical curves: type A depicting the irreversible one-electron process (Equations (1), (2), (4), and (5)) leading to $O_2^{\bullet-}$ scavenging, and type B depicting the irreversible two-electron process observed in

electro–chemical–electro reactions (Equations (1)–(3)). Figure 2 shows the plausible electrochemical mechanisms of $O_2/O_2^{\bullet-}$ in the presence of (a) $12H_2NQ$ and (b) $13H_2NQ$. These results summarize Equations (1)–(5).

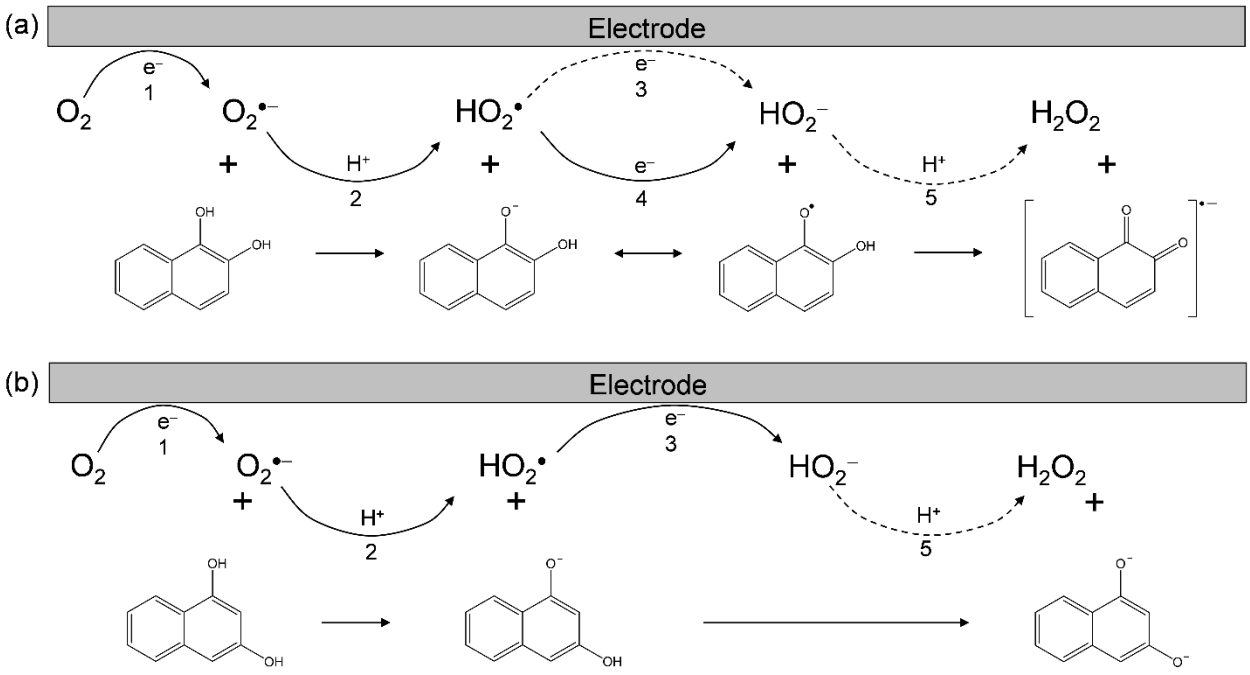

Figure 2. Plausible electrochemical mechanisms of $O_2/O_2^{\bullet-}$ in the presence of (a) $12H_2NQ$, and (b) $13H_2NQ$ in DMF. [1]One-electron reduction of $O_2/O_2^{\bullet-}$, [2]the initial proton transfer from the acidic substrate to $O_2^{\bullet-}$, [3]one-electron reduction of $HO_2^{\bullet}/HO_2^{-}$, [4]electron transfer from the substrate anion to $HO_2^{\bullet}$, [5]the second proton transfer to HO_2^{-}.

In this scenario, the CV result (Figure 1) recorded in the presence of $13H_2NQ$ was type B, indicating the absence of $O_2^{\bullet-}$ scavenging and the appearance of a cathodic-current-ascribed $HO_2^{\bullet}$. Conversely, the CV results in the presence of $12H_2NQ$ and $14H_2NQ$ were type A, indicating the scavenging of $O_2^{\bullet-}/HO_2^{\bullet}$ through the PCET involving two PTs and one ET (Figure 2). The reversible peaks (3c/3a and 4c/4a in Figure 1ac) appeared in these CV profiles are mainly assigned to two-step one-electron redox couples of the product radicals, $NQ/NQ^{\bullet-}$ and $NQ^{\bullet-}/NQ^{2-}$, respectively. Notably, the peak 3c was observed at the positive side of peak 1c ($O_2/O_2^{\bullet-}$) in the initial cathodic scan, before the initial electrogeneration of

$O_2^{\bullet-}$ that triggers a series of PCET reactions. Additionally, the cathodic current of the peak 1c decreases with a concentration dependency of the added H_2NQ, showing a consumption of O_2 (grayscale in Figure 1ac). The decrease in the peak 1c with the appearance of the peak 3c can be explained by a positive-shift of the redox potential of $O_2/O_2^{\bullet-}$ due to a hydrogen-bond (HB) preformed between O_2 and H_2NQ. That is, the cathodic peak 3c observed in Figure 1 at (a) –0.9 and (c) –1.1 V involves two reactions; the one-electron reduction of the O_2–H_2NQ complex, and the one-electron reduction of NQ that is produced in the solution through the PCET and the subsequent ET between $NQ^{\bullet-}$ and O_2 (Equation (6)). Along these series of reactions, the $O_2^{\bullet-}$ scavenging through the PCET and the subsequent $O_2^{\bullet-}$ generation, H_2O_2 formation from O_2 is catalyzed by H_2NQ in a superior kinetics as observed in the CV time scale. These CV profiles of $O_2/O_2^{\bullet-}$ are characteristic to that in the presence of $12H_2NQ$ or $14H_2NQ$, and cannot be observed in the presence of catechol,[22] hydroquinone,[23] and other antioxidants composed of substituted monophenols.[28,29,36,37] Thus, the CV results suggest that the planar naphthalene ring makes the ET feasible, generating $O_2^{\bullet-}$ and NQ from O_2 and $NQ^{\bullet-}$.

$$12NQ^{\bullet-} + O_2 \rightarrow 12NQ + O_2^{\bullet-} \qquad \text{ET} \qquad (6)$$

3.2 In situ electrolytic ESR spectral analyses of $O_2/O_2^{\bullet-}$ in the presence of $1nH_2NQ$

To confirm the PCET reaction between $O_2^{\bullet-}$ and $1nH_2NQ$, the CV solutions were analyzed by electrolytic ESR (scanning time = 4 minutes) in an in situ cell (Supporting Information, Figure S1). The spectra were acquired under an applied potential of −1.3 V, which corresponds to the electrogeneration of $O_2^{\bullet-}$ (Equation (1)). The ESR spectra were obtained only in the presence of $12H_2NQ$ and $14H_2NQ$. Figure 3 shows the ESR spectra of $O_2/O_2^{\bullet-}$ solution in the presence of (a-1) $12H_2NQ$ and (b-1) $14H_2NQ$. Then, hyperfine coupling constants for hydrogen (a_H/mT) were obtained by simulation based on the measured ESR spectra. Next, charges distributed on the structures of the product radicals, (a-2) $12NQ^{\bullet-}$ and (b-2) $14NQ^{\bullet-}$, were calculated using the DFT-(U)B3LYP/PCM/6-311+G(d,p) with the NBO

analysis, and the charges on carbons bonded to hydrogen were denoted. Considering the calculation results, the simulated a_H were assigned to their hydrogen of their substrate radical anions, $12NQ^{\bullet-}$ (H^a–H^f: 0.420, 0.050, 0.020, 0.137, 0.150, 0.010 mT) and $14NQ^{\bullet-}$ (H^a, H^b, H^c: 0.335, 0.035, 0.070 mT) formed through the PCET involving two PTs and one ET.

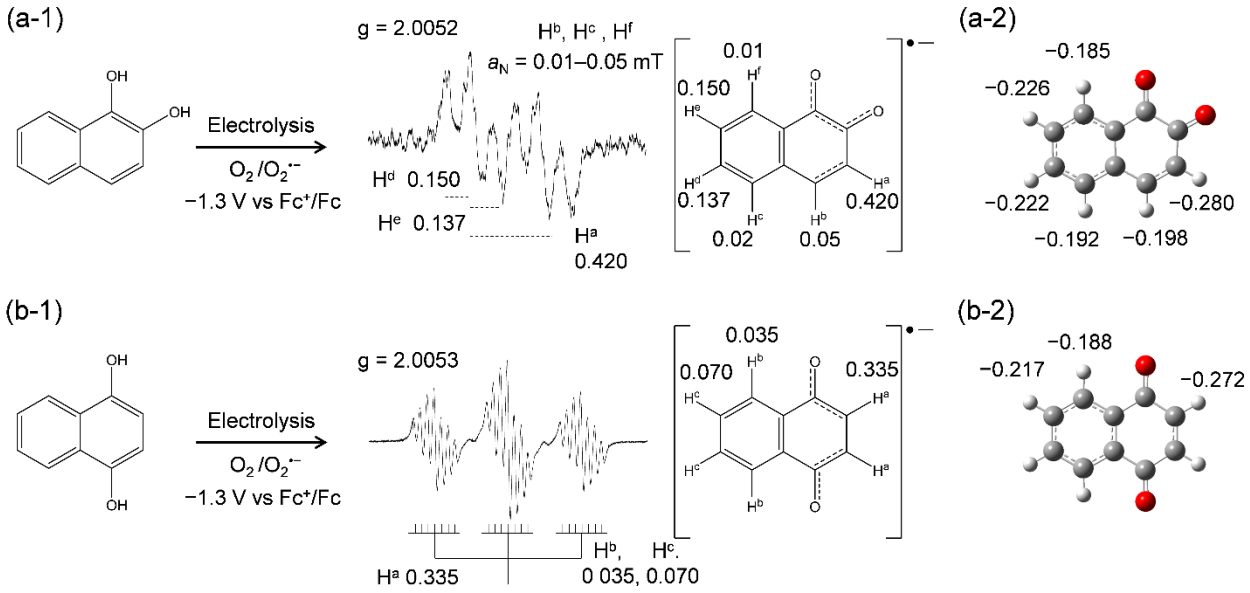

Figure 3. Electrolytic ESR spectra for O_2 (4.8×10^{-3} mol dm^{-3}) in DMF solutions in the presence of (a-1) $12H_2NQ$, and (b-1) $14H_2NQ$ at 5.0×10^{-3} mol dm^{-3} obtained by in situ controlled-potential electrolysis of solutions containing 0.1 mol dm^{-3} TPAP at an applied potential of −1.3 V vs Fc^+/Fc. Radical structures with the g-values and the appropriate hyperfine coupling constants for hydrogen (a_H/mT) were obtained by simulation based on the measured spectra. The charge distributions on the carbons bonded to hydrogen for (b-1) $12NQ^{\bullet-}$, and (b-2) $14NQ^{\bullet-}$ were calculated using the DFT-(U)B3LYP/PCM/6-311+G(d,p) with the NBO analysis.

3.3 DFT analysis on change in HOMO–LUMO energies during PCET between $12H_2NQ$/$14H_2NQ$ and $O_2^{\bullet-}$

The mechanistic analysis of $O_2^{\bullet-}$ scavenging by $12H_2NQ$/$14H_2NQ$ in DMF was supplemented by a DFT-based frontier molecular-orbital analysis with the B3LYP hybrid functional. Figure 4 shows the HOMO–LUMO changes during the PCET. After the initial PT,

the reactant species $12H_2NQ/14H_2NQ$, $12HNQ^-/14H_2NQ^-$, $O_2^{\bullet-}$, and $HO_2^\bullet$ coexisted in the solution. The singly occupied molecular orbital (SOMO) energy of $HO_2^\bullet$ (−0.31659 a.u.) was much lower than the HOMO energies of $1nH_2NQ$ ($12H_2NQ$:−0.21100 a.u., $14H_2NQ$:−0.20679 a.u.) and its anion ($12HNQ^-$:−0.16268 a.u., $14HNQ^-$:−0.15465 a.u.), indicating that the electron acceptor was $HO_2^\bullet$ rather than $O_2^{\bullet-}$. Meanwhile, the CV in DMF revealed that $HO_2^\bullet$ formed after the initial PT was scavenged (Figure 1ac). Therefore, the electron donor was the anions (the downhill energy relationship during the ET is indicated by the bold red lines in Figure 4). These changes in HOMO–LUMO energies occur during the PT between $12H_2NQ/14H_2NQ$ and $O_2^{\bullet-}$, which forms $12HNQ^-/14HNQ^-$ and $HO_2^\bullet$. After the subsequent ET, the HOMO–LUMO relationship between the products is reversed and the orbital energies change along the red dotted lines in Figure 4. However, as the PT-forming H_2O_2 has a lower HOMO (−0.27731 a.u.) than HO_2^- (−0.16694 a.u.), the reverse ET cannot proceed so the ET direction is dominantly determined by the subsequent PT. Judging from the HOMO–LUMO relationship for $O_2^{\bullet-}$ scavenging by $12H_2NQ/14H_2NQ$, the net PCET involves two PTs and one ET.

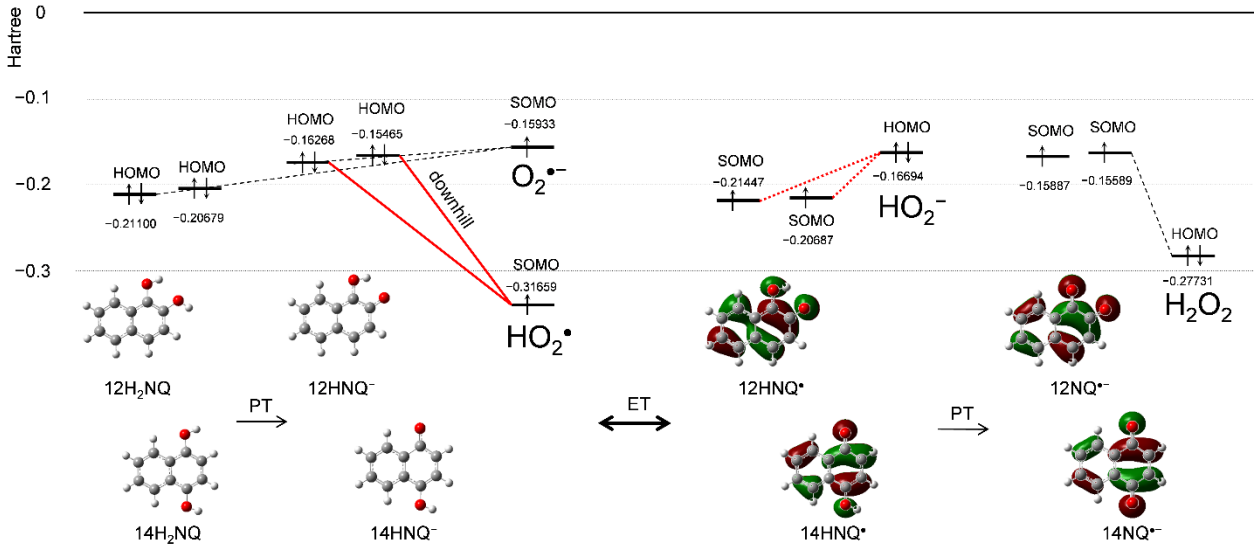

Figure 4. Change in HOMO−LUMO energies (hartree/a.u.) during PCET between $12H_2NQ/14H_2NQ$ and $O_2^{\bullet-}$ with its corresponding chemical species in DMF, calculated using the DFT-(U)B3LYP/PCM/6-311+G(d,p).

3.4 Free energy calculations of PCET between 1*n*H_2NQ and $O_2^{\bullet-}$

For a mechanistic analysis of $O_2^{\bullet-}$ scavenging by 1*n*H_2NQ in DMF, DFT calculations were performed at the (U)B3LYP/PCM/6-311+G(d,p) level. Figure 5 shows the equilibrium schemes and standard Gibbs free energy changes ($\Delta G°$/kJ mol^{-1}, 298.15 K) of the six diabatic electronic states in the PCET involving two PTs and one ET between (a) $O_2^{\bullet-}$ and 12H_2NQ, and (b) $O_2^{\bullet-}$ and 14H_2NQ. The main drivers of these sequential processes are the $\Delta G°$s of the individual reactions, the acid–base interaction, and the redox potentials of the components. As ET1 (a: 359.0, b: 345.9) in Figure 5 is strongly endergonic, PT1 (a: 21.2, b: 40.7) dominantly forms 12HNQ$^-$/14NQ$^-$ and $HO_2^{\bullet}$. In the following pathway (bottom part of the panels in Figure 5ab), PT3 (a: 388.7, b: 361.2) is uphill endergonic, so ET2 (a: 1.2, b: −17.6) is likely to proceed. Notably in Figure 5, PT4 is exergonic (a: −78.5, b: −95.3), meaning that two PTs must be coupled to one ET for successful $O_2^{\bullet-}$ scavenging. This suggests that the initial PT (PT1) is dominant in the subsequent ET2–PT4. Another feasible pathway is one-step one ET concerted with sequential two-PT after initial formation of the prereactive complex (PRC) via HBs between 12H_2NQ/14H_2NQ and $O_2^{\bullet-}$ without generating high energy intermediates. We refer to this pathway as the concerted two-proton-coupled electron transfer (2PCET) reaction.[22,34]

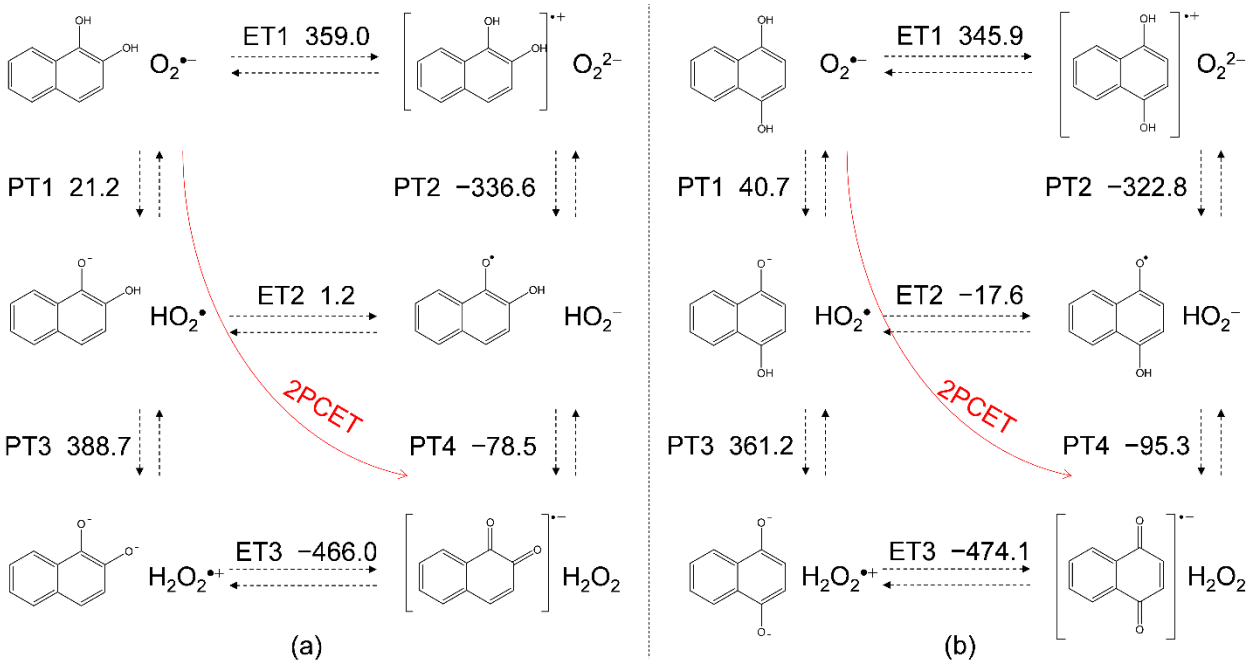

Figure 5. Six diabatic electronic states and the $\Delta G°$ values of PCET between (a) $12H_2NQ$ and $O_2^{\bullet-}$, and (b) $14H_2NQ$ and $O_2^{\bullet-}$ in DMF, involving two proton-transfers (PT) and one electron-transfer (ET). The $\Delta G°$s (kJ mol^{-1}, 298.15 K) of (PT1–PT4) and ET (ET1–ET3) were calculated using the DFT-(U)B3LYP/PCM/6-311+G(d,p) method.

For a comparative study, the $\Delta G°$ values of the PCET pathways of $1nH_2NQ$ including $13H_2NQ$ were calculated using three functionals, B3LYP, ω-B97XD, and M06-2X, (Table 1). From a thermodynamic viewpoint, the energetic driving force of the PCET is the $\Delta G°$ of the net PCET, obtained by summing the $\Delta G°$s of the two PTs and one ET. If the PCET occurs along a pathway involving an infeasible single PT/ET, the total $\Delta G°$ cannot embody the energetic driving force because it includes the $\Delta G°$ of the infeasible PT/ET. Along the plausible pathway for $13H_2NQ$, the initial PT1 and the subsequent ET2 were both endergonic, using any of the functional shown in Table 1. Conversely, the total $\Delta G°$ for $14H_2NQ$ embodies the exergonic driving force, because ET2 after the initial PT1 is exergonic. On the other hand, the $\Delta G°$ values of the sequential PCET pathway of $12H_2NQ$, PT1–ET2–PT4, cannot be evaluated correctly because the optimized structure of intermediates after PT1 ($12HNQ^-$) and ET2 ($12HNQ^{\bullet}$) are stabilized by their intramolecular HB formed among the

two carbonyl-oxygen-atoms. These results are independent of the computational method, three density functionals yielding similar energies for the PCET. However, the highest energies for ET2 are obtained using the M06-2X functional (12H_2NQ:18.2, 13H_2NQ:37.2, 14H_2NQ:−0.2), while M06-2X was parameterized taking into account HAT reactions involving PCET.[34] Considering above, the 2PCET rather than the sequential PCET is plausible pathway for 12H_2NQ and 14H_2NQ, indicating that the ortho- and para- resonance structure confers the exergonic total $\Delta G°$s (−55.3, −69.9), which consistent with the electrochemical results on CV time scales (Figures 1–3).

Table 1. ΔG^o values (kJ mol^{-1}, 298.15 K) of proton-coupled electron transfer between $O_2^{\bullet-}$ and 1*n*H_2NQ in DMF, calculated using DFT at the B3LYP, ω-B97XD, and M06-2X functionals, in conjunction with the PCM/6-311+G(d,p) basis set.

	Compounds	PT1	PT2	PT3	PT4	ET1	ET2	ET3	[1]Total
B3LYP	12H_2NQ	21.2	−336.6	388.7	−78.5	359.0	1.2	−466.0	−56.1
	13H_2NQ	35.5	−315.5	337.1	−77.8	367.0	16.0	−398.9	−26.3
	14H_2NQ	40.7	−322.8	361.2	−95.3	345.9	−17.6	−474.1	−72.2
ω-B97XD	12H_2NQ	22.2	−343.1	388.3	−84.1	376.2	10.7	−461.7	−51.1
	13H_2NQ	34.6	−323.6	334.8	−81.9	386.6	28.4	−388.2	−18.9
	14H_2NQ	40.7	−330.6	361.1	−99.2	362.5	−8.2	−468.5	−66.7
M06-2X	12H_2NQ	19.9	−361.5	391.5	−93.4	399.6	18.2	−466.7	−55.3
	13H_2NQ	32.2	−342.1	339.2	−84.6	411.5	37.2	−386.6	−15.2
	14H_2NQ	38.4	−346.9	365.4	−108.1	385.1	−0.2	−473.7	−69.9

[1] Total values involve the sum of ΔG^os for two proton-transfers (PT) and one electron-transfer (ET).

3.6 Potential-energy surfaces of the PCET between 12H_2NQ and $O_2^{\bullet-}$

To gain deeper insight into the PCET mechanism of $O_2^{\bullet-}$ scavenging by $12H_2NQ$ in DMF, the potential-energy surfaces were investigated at the (U)B3LYP/PCM/6-311+G(d,p) level of theory. The reaction is assumed to proceed by three elementary steps: i) formation of the PRC via HBs from the free reactants, ii) 2PCET reaction forming the product complex (PC) via a TS, and iii) dissociation of the PC yielding the free products (Supplementary Materials, Table S2). The structural and electronic changes during the reaction were analyzed through NBO calculations. We first performed a potential-energy scanning of the stable HB complexes (PRC, the intermediate HB complex, and the PC) along the PCET reaction (Figure 6a). We then optimized the structures of the plausible PRCs ($12H_2NQ$–$O_2^{\bullet-}$) formed from the free reactants ($12H_2NQ$ and $O_2^{\bullet-}$) via two HBs (step i). After optimization, the $\Delta G°$ reduced by 31.0 kJ mol^{-1} (the $\Delta G°$ of the PRC was set to zero in Figure 6a). Next, we constructed the energy profile ($\Delta G°$, kJ mol^{-1}) along the IRC for the 2PCET involving concerted two PTs and one ET, which forms the PC ($12NQ^{\bullet-}$–H_2O_2) (step ii). The IRC revealed a 2PCET between $12H_2NQ$ and $O_2^{\bullet-}$ in one-kinetic process via a TS and no generation of intermediates such as $HO_2^{\bullet}$, HO_2^{-}, $12HNQ^{-}$, and $12HNQ^{\bullet}$. Although the IRC is similar to that for catechol (Supplementary Materials, Figure S2), obtained activation energy (E_a = 41.1 kJ mol^{-1}) was lower than those for 2PCET between $O_2^{\bullet-}$ and catechol derivatives (catechol: 52.3, benzene-1,2,3-triol: 53.5, and 3-methoxybenzen-1,2-diol: 50.8) by about 10 kJ mol^{-1},[22,36] indicating that the naphthalene ring of $12H_2NQ$ kinetically promotes the 2PCET. The obtained E_a value is in agreement with the electrochemical result, showing the superior kinetics of the 2PCET.

Figure 6b shows the dependence of O−H bond distance (OH^1: black line, and OH^2: red line) on the number of electrons in the π-orbital of the planar molecule of $12H_2NQ$ along the IRC (blue circles). The spin density distributions were localized on the radicals before and after the TS along the 2PCET, showing that the radical localized on $O_2^{\bullet-}$ in the initial PRC was transferred to $12NQ^{\bullet-}$ in the resulting PC. The spin changes on the electron-donor side

(12H_2NQ) and electron-acceptor side ($O_2^{\bullet-}$) were well correlated with the changes in the π-electrons of 12H_2NQ. Furthermore, after carefully observing the changes in structures and OH^1/OH^2 in the IRC, one finds that π-electron transfer occurs simultaneously with sequential lengthening of the two O–H bond distances. In the first step of the reaction, one proton (H^1) is attracted by $O_2^{\bullet-}$. This attraction results in nearly complete deprotonation of 12H_2NQ and the transfer of one-half of the π-electrons from 12H_2NQ to $O_2^{\bullet-}$ in the TS. Movement of the second proton (H^2) accelerates the ET forward from the TS, eventually forming the PC as the resulting reaction system. The results also demonstrate that the TS is electronically characterized by delocalization of the radical anion over the HB complex of the components.

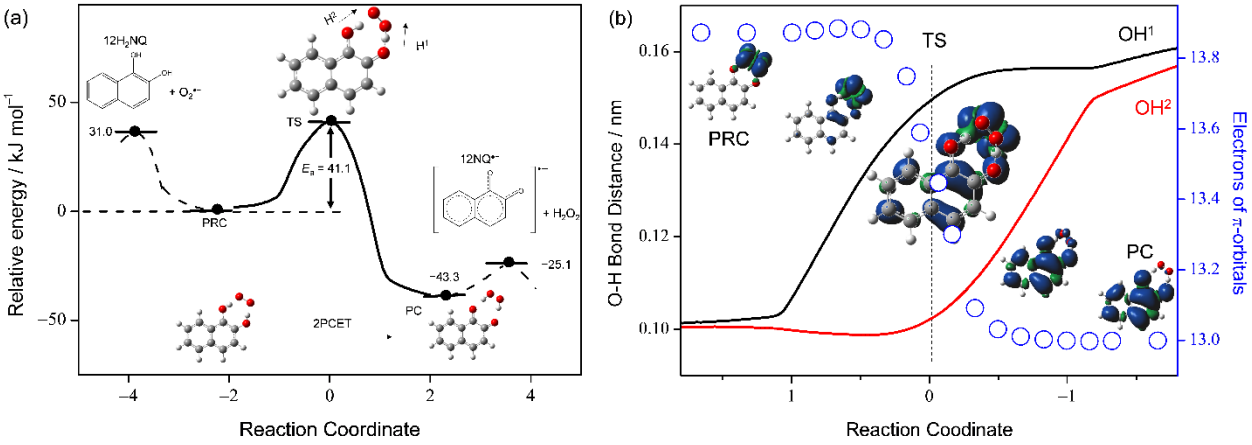

Figure 6. (a) Energy profile (kJ mol^{-1}) along the intrinsic reaction coordinate of concerted two-proton-coupled electron transfer between 12H_2NQ and $O_2^{\bullet-}$ in DMF, with the structures of free reactants (12H_2NQ, $O_2^{\bullet-}$), prereactive complex (PRC), transition state (TS), product complex (PC), and free products (12$NQ^{\bullet-}$, H_2O_2). (b) Left and right vertical axes represent the O–H bond distances (OH^1: black line, OH^2: red line, nm) and the number of electrons (open circles) in the π-orbitals of 12H_2NQ, respectively. Calculations were performed using the DFT-(U)B3LYP/PCM/6-311+G(d,p) method.

Collectively, these findings indicate that $O_2^{\bullet-}$ scavenging by 12H_2NQ in DMF is governed by the 2PCET after forming PRC via two HBs, which corresponds to moving along the red diagonal lines of the two panels in Figure 5a. A similar 2PCET mechanism is inferred for the

reaction between $O_2^{\bullet-}$ and $14H_2NQ$, among an extensive HB network via the para-OHs alternately formed and broken with each of the neighboring $O_2^{\bullet-}$. Figure 7 shows the net reaction mechanism between electrogenerated (a) $O_2^{\bullet-}$ and $12H_2NQ$, and (b) $O_2^{\bullet-}$ and $14H_2NQ$ in DMF. In the 2PCET mechanism, ET occurs between the oxygen π orbitals orthogonal to the molecular frameworks of the donor and accepter, then, PT occurs between the oxygen σ orbitals along the HBs.[22,34,36] Numbers of spin distributed on the NQ planar molecule, a quinoid subunit (A ring) and a fused aromatic ring (B ring), are also given in Figure 7. Notably, the spins are distributed on the B ring of the product radical ($12NQ^{\bullet-}$:0.123, $14NQ^{\bullet-}$:0.085) that expands the π-conjugated plane, demonstrating that the radical product is more stabilized than the mono-ring-quinone radicals generated from catechol and hydroquinone. These results showed that the B ring of NQ thermodynamically promotes the net PCET mechanism. Furthermore, the stability of the $NQ^{\bullet-}$ leads to the subsequent generation of $O_2^{\bullet-}$ (Equation (6)) under aerobic conditions.

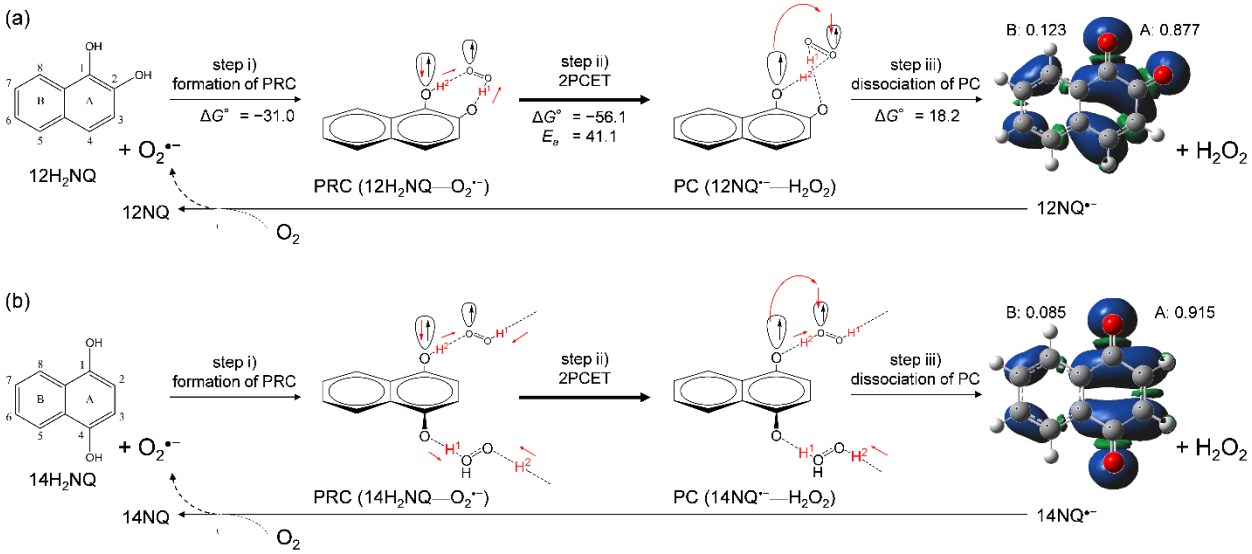

Figure 7. Plausible mechanisms with $\Delta G°$ and E_a values (kJ mol^{-1}, 298.15 K) of the reactions between (a) $12H_2NQ$ and $O_2^{\bullet-}$, and (b) $14H_2NQ$ and $O_2^{\bullet-}$ in DMF, (step i) formation of prereactive complex (PRC), (step ii) concerted two-proton-coupled electron transfer (2PCET), (step iii) dissociation of product complex (PC), and subsequent electron transfer between

product radical (a:12NQ$^{\bullet-}$, b:14NQ$^{\bullet-}$) and O_2 generating naphthoquinone (a:12NQ, b:14NQ) and $O_2^{\bullet-}$. The $\Delta G°$ and E_a values were calculated using the DFT-(U)B3LYP/PCM/6-311+G(d,p) method. Spin numbers distributed on two rings (A, B) of the product radical were obtained by NBO analysis.

4 Conclusions

In this study, we derived the reactivities of 1*n*H_2NQ toward $O_2^{\bullet-}$ in DMF. The main findings are summarized below.

- 12H_2NQ and 14H_2NQ scavenge $O_2^{\bullet-}$ forming H_2O_2 through a 2PCET involving concerted two PTs and one ET. This reaction is mediated by the ortho- or para-resonance moiety.
- $O_2^{\bullet-}$ generation via the subsequent ET between product-NQ$^{\bullet-}$ and O_2 was electrochemically observed.
- The naphthalene ring contributes to the thermodynamic stability of the product radical, the superior kinetics (E_a) of the 2PCET mechanism for a successful $O_2^{\bullet-}$ scavenging, and the subsequent generation of $O_2^{\bullet-}$ from O_2 and product-NQ$^{\bullet-}$.
- Along the $O_2^{\bullet-}$ scavenging through the 2PCET and the subsequent $O_2^{\bullet-}$ generation by the product-NQ$^{\bullet-}$, H_2O_2 formation from O_2 is catalyzed by H_2NQ.

Although the presented results are specific to chemical reactions in aprotic DMF solvent, the PCET theory is adaptable to biological processes in biotic structures such as lipid bilayers. Therefore, we hope that the findings will reveal the mechanistic actions of the scavenging and generation of $O_2^{\bullet-}$ by 1*n*H_2NQ, thus securing its pharmacological use as an anticancer agent.

Supporting Information

brief description (PDF)

Corresponding Author

*Tatsushi Nakayama

ORCID: 0000-0002-0346-2089

E-mail: tnakayama@gifu-pu.ac.jp

Phone No: +81-58-230-8100

Fax No: +81-58-230-8200

Funding Sources

This research was funded by a Grant-in-Aid for Scientific Research, grant number 19K16338, from the Japan Society for the Promotion of Science (JSPS).

ACKNOWLEDGMENT

The authors want to thank Yuki Mori and Norimi Kobayashi for their experimental assistance.

REFERENCES

(1) Di Gennaro, P.; Bestetti, G.; Galli, E.; Orsini, F.; Pelizzoni, F.; Sello, G. Bioconversion of Substituted Naphthalenes to the Corresponding 1,2-Dihydro Derivatives by Escherichia Coli Recombinant Strains. *Tetrahedron Lett.* **1997**, *38* (35), 6267–6270. https://doi.org/10.1016/S0040-4039(97)01404-4.

(2) González, F. J. Cyclic Voltammetry of Two Analogue K-Group Vitamin Compounds in Dimethylsulfoxide. *Electroanalysis* **1998**, *10* (9), 638–642. https://doi.org/10.1002/(SICI)1521-4109(199807)10:9<638::AID-ELAN638>3.0.CO;2-R.

(3) Frontana, C. E.; González, I. Structural Factors Affecting the Reactivity of the Natural A-Hydroxy Benzoquinones. An Electrochemical and ESR Study. *ECS Trans.* **2007**, *3* (29), 13–23. https://doi.org/10.1149/1.2753287.

(4) Chaturvedi, A. K.; Rastogi, N. Unsaturated Phosphonates as Hauser Acceptors for the Synthesis of Phosphonylated Dihydroxynaphthalenes and Naphthoquinones. *J. Org. Chem.* **2016**, *81* (8), 3303–3312. https://doi.org/10.1021/acs.joc.6b00312.

(5) Kayashima, T.; Mori, M.; Yoshida, H.; Mizushina, Y.; Matsubara, K. 1,4-Naphthoquinone Is a Potent Inhibitor of Human Cancer Cell Growth and Angiogenesis. *Cancer Lett.* **2009**, *278* (1), 34–40. https://doi.org/10.1016/j.canlet.2008.12.020.

(6) Pereyra, C. E.; Dantas, R. F.; Ferreira, S. B.; Gomes, L. P.; Silva, F. P. The Diverse Mechanisms and Anticancer Potential of Naphthoquinones. *Cancer Cell Int.* **2019**, *19* (207). https://doi.org/10.1186/s12935-019-0925-8.

(7) Goulart, M. O. F.; Falkowski, P.; Ossowski, T.; Liwo, A. Electrochemical Study of Oxygen Interaction with Lapachol and Its Radical Anions. *Bioelectrochemistry* **2003**, *59* (1–2), 85–87. https://doi.org/10.1016/S1567-5394(03)00005-7.

(8) Zhang, Y.; Luo, Y. H.; Piao, X. J.; Shen, G. N.; Wang, J. R.; Feng, Y. C.; Li, J. Q.; Xu, W. T.; Zhang, Y.; Zhang, T.; Wang, C. Y.; Jin, C. H. The Design of 1,4-Naphthoquinone Derivatives and Mechanisms Underlying Apoptosis Induction through ROS-Dependent MAPK/Akt/STAT3 Pathways in Human Lung Cancer Cells. *Bioorg. Med. Chem.* **2019**, *27* (8), 1577–1587. https://doi.org/10.1016/J.BMC.2019.03.002.

(9) Murakami, K.; Haneda, M.; Iwata, S.; Yoshino, M. Effect of Hydroxy Substituent on the Prooxidant Action of Naphthoquinone Compounds. *Toxicol. Vitr.* **2010**, *24* (3), 905–909. https://doi.org/10.1016/j.tiv.2009.11.018.

(10) Silva, L. R.; Guimarães, A. S.; do Nascimento, J.; do Santos Nascimento, I. J.; da Silva, E. B.; McKerrow, J. H.; Cardoso, S. H.; da Silva-Júnior, E. F. Computer-Aided Design of 1,4-Naphthoquinone-Based Inhibitors Targeting Cruzain and Rhodesain Cysteine Proteases. *Bioorg. Med. Chem.* **2021**, *41*, 116213. https://doi.org/10.1016/J.BMC.2021.116213.

(11) Asche, C. Antitumour Quinones. *Mini-Reviews Med. Chem.* **2005**, *5* (5), 449–467. https://doi.org/10.2174/1389557053765556.

(12) Ferreira, F. D. R.; Ferreira, S. B.; Araújo, A. J.; Marinho Filho, J. D. B.; Pessoa, C.; Moraes, M. O.; Costa-Lotufo, L. V.; Montenegro, R. C.; Da Silva, F. D. C.; Ferreira, V. F.; Da Costa, J. G.; De Abreu, F. C.; Goulart, M. O. F. Arylated α- And β-Dihydrofuran Naphthoquinones: Electrochemical Parameters, Evaluation of Antitumor Activity and Their Correlation. *Electrochim. Acta* **2013**, *110*, 634–640. https://doi.org/10.1016/j.electacta.2013.04.148.

(13) Hlavata, L.; Benikova, K.; Vyskocil, V.; Labuda, J. Evaluation of Damage to DNA Induced by UV-C Radiation and Chemical Agents Using Electrochemical Biosensor Based on Low Molecular Weight DNA and Screen-Printed Carbon Electrode. *Electrochim. Acta* **2012**, *71*. https://doi.org/10.1016/j.electacta.2012.03.119.

(14) Dixon, S. J.; Lemberg, K. M.; Lamprecht, M. R.; Skouta, R.; Zaitsev, E. M.; Gleason, C. E.; Patel, D. N.; Bauer, A. J.; Cantley, A. M.; Yang, W. S.; Morrison, B.; Stockwell, B. R. Ferroptosis: An Iron-Dependent Form of Nonapoptotic Cell Death. *Cell* **2012**, *149* (5). https://doi.org/10.1016/j.cell.2012.03.042.

(15) Ferreira, F. D. R.; Ferreira, S. B.; Araújo, A. J.; Marinho Filho, J. D. B.; Pessoa, C.; Moraes, M. O.; Costa-Lotufo, L. V.; Montenegro, R. C.; Da Silva, F. D. C.; Ferreira, V.

F.; Da Costa, J. G.; De Abreu, F. C.; Goulart, M. O. F. Arylated α- and β-Dihydrofuran Naphthoquinones: Electrochemical Parameters, Evaluation of Antitumor Activity and Their Correlation. *Electrochim. Acta* **2013**, *110*, 634–640. https://doi.org/10.1016/J.ELECTACTA.2013.04.148.

(16) Schopfer, P.; Heyno, E.; Drepper, F.; Krieger-Liszkay, A. Naphthoquinone-Dependent Generation of Superoxide Radicals by Quinone Reductase Isolated from the Plasma Membrane of Soybean. *Plant Physiol.* **2008**, *147* (2), 864–878. https://doi.org/10.1104/pp.108.118745.

(17) Singh, S. K.; Husain, S. M. A Redox-Based Superoxide Generation System Using Quinone/Quinone Reductase. *ChemBioChem* **2018**, *19* (15), 1657–1663. https://doi.org/10.1002/cbic.201800071.

(18) Nanni, E. J.; Birge, R. R.; Hubbard, L. M.; Morrison, M. M.; Sawyer, D. T. Oxidation and Dismutation of Superoxide Ion Solutions to Molecular Oxygen. Singlet vs. Triplet State. *Inorg. Chem.* **1981**, *20* (3), 737–741. https://doi.org/10.1021/ic50217a019.

(19) Nanni, E. J.; Stallings, M. D.; Sawyer, D. T. Does Superoxide Ion Oxidize Catechol, α-Tocopherol, and Ascorbic Acid by Direct Electron Transfer? *J. Am. Chem. Soc.* **1980**, *102* (13), 4481–4485. https://doi.org/10.1021/ja00533a029.

(20) Song, C.; Zhang, J. Electrocatalytic Oxygen Reduction Reaction. In *PEM Fuel Cell Electrocatalysts and Catalyst Layers: Fundamentals and Applications*; Springer: Berlin, Germany: Berlin, 2008; pp 89–134. https://doi.org/10.1007/978-1-84800-936-3_2.

(21) Singh, P. S.; Evans, D. H. Study of the Electrochemical Reduction of Dioxygen in Acetonitrile in the Presence of Weak Acids. *J. Phys. Chem. B* **2006**, *110*, 637–644. https://doi.org/10.1021/jp055296f.

(22) Nakayama, T.; Uno, B. Concerted Two-Proton-Coupled Electron Transfer from Catechols to Superoxide via Hydrogen Bonds. *Electrochim. Acta* **2016**, *208*, 304–309. https://doi.org/10.1016/j.electacta.2016.05.034.

(23) Nakayama, T.; Uno, B. Quinone-Hydroquinone π-Conjugated Redox Reaction Involving Proton-Coupled Electron Transfer Plays an Important Role in Scavenging Superoxide by Polyphenolic Antioxidants. *Chem. Lett.* **2010**, *39* (3), 162–164. https://doi.org/10.1246/cl.2010.162.

(24) Nakayama, T.; Uno, B. Importance of Proton-Coupled Electron Transfer from Natural Phenolic Compounds in Superoxide Scavenging. *Chem. Pharm. Bull. (Tokyo).* **2015**, *63* (12), 967–973. https://doi.org/10.1248/cpb.c15-00447.

(25) Nakayama, T.; Uno, B. Structural Properties of 4-Substituted Phenols Capable of Proton-Coupled Electron Transfer to Superoxide. *Int. J. Adv. Res. Chem. Sci.* **2016**, *3* (1), 11–19. https://doi.org/10.20431/2349-0403.0301002.

(26) Biela, M.; Rimarčík, J.; Senajová, E.; Kleinová, A.; Klein, E. Antioxidant Action of Deprotonated Flavonoids: Thermodynamics of Sequential Proton-Loss Electron-Transfer. *Phytochemistry* **2020**, *180* (112528). https://doi.org/10.1016/j.phytochem.2020.112528.

(27) Fridovich, I. Superoxide Dismutase. In *Encyclopedia of Biological Chemistry: Second Edition*; Elsevier Inc., 2013; pp 352–354. https://doi.org/10.1016/B978-0-12-378630-2.00129-8.

(28) Nakayama, T.; Honda, R. Electrochemical and Mechanistic Study of Superoxide Elimination by Mesalazine through Proton-Coupled Electron Transfer. *Pharmaceuticals* **2021**, *14* (2), 120. https://doi.org/10.3390/ph14020120.

(29) Nakayama, T.; Honda, R.; Kuwata, K.; Usui, S.; Uno, B. Electrochemical and Mechanistic Study of Reactivities of α-, β-, γ-, and δ-Tocopherol toward Electrogenerated Superoxide in N,N-Dimethylformamide through Proton-Coupled Electron Transfer. *Antioxidants* **2022**, *11* (1), 115–128. https://doi.org/10.3390/antiox11010009.

(30) Okumura, N.; Uno, B. Electronic Spectra of the Electrogenerated 1,4-Benzoquinone π-Dianion and the Strongly Hydrogen-Bonded Charge-Transfer Complex with Methanol. *Bull. Chem. Soc. Jpn.* **1999**, *72* (6), 1213–1217. https://doi.org/10.1246/bcsj.72.1213.

(31) Becke, A. D. Density-Functional Thermochemistry. V. Systematic Optimization of Exchange-Correlation Functionals. *J. Chem. Phys.* **1997**, *107* (20), 8554–8560. https://doi.org/10.1063/1.475007.

(32) Zhao, Y.; Truhlar, D. G. The M06 Suite of Density Functionals for Main Group Thermochemistry, Thermochemical Kinetics, Noncovalent Interactions, Excited States, and Transition Elements: Two New Functionals and Systematic Testing of Four M06-Class Functionals and 12 Other Function. *Theor. Chem. Acc.* **2008**, *120* (1–3), 215–241. https://doi.org/10.1007/s00214-007-0310-x.

(33) Frisch G. W.; Schlegel, H. B.; Scuseria, G. E.; Robb, M. A.; Cheeseman, J. R.; Scalmani, G.; Barone, V.; Petersson, G. A.; Nakatsuji, H.; Li, X.; Caricato, M.; Marenich, A. V.; Bloino, J.; Janesko, B. G.; Gomperts, R.; Mennucci, B.; Hratch, D. J., M. J. . T. *Gaussian 16, Rev. B.01*; Gaussian, Inc.: Wallingford, CT, USA, 2016. https://doi.org/111.

(34) Quintero-Saumeth, J.; Rincón, D. A.; Doerr, M.; Daza, M. C. Concerted Double Proton-Transfer Electron-Transfer between Catechol and Superoxide Radical Anion. *Phys. Chem. Chem. Phys.* **2017**, *19* (38), 26179–26190. https://doi.org/10.1039/c7cp03930a.

(35) Reed, A. E.; Weinstock, R. B.; Weinhold, F. Natural Population Analysis. *J. Chem. Phys.* **1985**, *83* (2), 735–746. https://doi.org/10.1063/1.449486.

(36) Nakayama, T.; Honda, R.; Kuwata, K.; Usui, S.; Uno, B. Electrochemical and Mechanistic Study of Superoxide Scavenging by Pyrogallol in N,N-Dimethylformamide through Proton-Coupled Electron Transfer. *Electrochem* **2022**, *3* (1), 115–128. https://doi.org/doi.org/10.3390/electrochem3010008.

(37) René, A.; Abasq, M. L.; Hauchard, D.; Hapiot, P. How Do Phenolic Compounds React toward Superoxide Ion? A Simple Electrochemical Method for Evaluating Antioxidant Capacity. *Anal. Chem.* **2010**, *82* (20), 8703–8710. https://doi.org/10.1021/ac101854w.